Article:
Karageorghis, A., Lesnic, D. and Marin, L. (2024) Solution of Inverse Geometric Problems Using a Non-Iterative MFS. Communications in Computational Physics, 35 (3). pp. 553-578. ISSN: 1815-2406

https://doi.org/10.4208/cicp.OA-2023-0207

SOLUTION OF INVERSE GEOMETRIC PROBLEMS USING A NON-ITERATIVE MFS

ANDREAS KARAGEORGHIS, DANIEL LESNIC, AND LIVIU MARIN

Abstract. In most of the method of fundamental solutions (MFS) approaches employed so far for the solution of inverse geometric problems, the MFS implementation typically leads to non–linear systems which were solved by standard nonlinear iterative least squares software. In the current approach, we apply a three–step non–iterative MFS technique for identifying a rigid inclusion from internal data measurements, which consists of: (i) a direct problem to calculate the solution at the set of measurement points, (ii) the solution of an ill–posed linear problem to determine the solution on a known virtual boundary and (iii) the solution of a direct problem in the virtual domain which leads to the identification of the unknown curve using the MATLAB® functions `contour` in 2D and `isosurface` in 3D. The results of several numerical experiments for steady–state heat conduction and linear elasticity in two and three dimensions are presented and analyzed.

1. Introduction

The method of fundamental solutions (MFS) has, in recent years, been used extensively for the solution of inverse geometric problems [7, 15]. This is because its main features (meshlessness and ease of application to problems in complex geometries in 2D and 3D) make it ideally suited for the solution of such problems in which the main dependent variable along with part of the boundary are unknown and have to be determined from some extra suitable measurements. The MFS formulations put forward in the literature typically lead to the solution of systems of nonlinear equations which require the use of standard nonlinear iterative software such as the MATLAB® routine `lsqnonlin`, the application of which can be quite costly. For the approach to become less costly, the Jacobian of the system needs to be calculated and provided which is rather tedious [19].

The objective of this paper is to extend the application of the MFS combined with a non-iterative level-set method for identifying a rigid inclusion from internal measurements in the fields of steady-state heat conduction and linear elasticity. Therefore, we shall consider inverse geometric problems of the type considered in [8,25,26] using the finite difference method, in [28] using the finite element method and [9,27] using the boundary element method (BEM). In particular, we shall follow closely the ideas and strategy developed in [27] which are based on the virtual area/volume concept, and adjust them to the MFS. The proposed method leads to the solution of an ill–conditioned system of linear equations to calculate the solution on the virtual boundary. This involves the pseudo–inverse of an ill–conditioned matrix which is calculated and regularized using the truncated

Date: January 2, 2024.

2000 *Mathematics Subject Classification.* Primary 65N35; Secondary 65N21, 65N38.

Key words and phrases. Void detection, inverse problem, method of fundamental solutions.

singular value decomposition (SVD). We assume that the unknown rigid inclusion is star–shaped and its boundary lies in a known annular domain in between the virtual boundary and a curve on which the internal measurements are situated. Then, the unknown boundary is subsequently recovered by searching for a specific iso–curve in two dimensions (2D) or a specific iso–surface in three dimensions (3D). These searches can be easily carried out utilizing the MATLAB® functions `contour` in 2D and `isosurface` in 3D. We should mention that the proposed method has some similarities to the Kirsch and Kress method [20, 21] proposed by [1], see also [2], for the solution of a different type of inverse geometric problems. This leads to another way of determining the solution on the virtual boundary and Tikhonov regularization [12, Section 4.4] is applied instead of the truncated SVD.

The type of problems to be solved is presented in Section 2. In Section 3 we describe in detail the application of the method in the three steps which lead to the determination of the unknown boundary. The results of several numerical experiments in 2D and 3D steady–state heat conduction and linear elasticity are analyzed in Sections 4 and 5. Finally, concluding remarks are given in Section 6.

2. Mathematical formulation

We consider the inverse boundary value problem (BVP) for the Laplace equation in $\mathbb{R}^2$ or $\mathbb{R}^3$ [27]

$$\Delta u = 0 \quad \text{in} \quad \Omega := \Omega_2 \backslash \overline{\Omega}_1, \tag{2.1a}$$

subject to the boundary conditions (BCs)

$$u = u_{\text{int}} \equiv \text{constant} \quad \text{on} \quad \partial\Omega_1 \tag{2.1b}$$

and

$$u = u_{\text{ext}} \not\equiv u_{\text{int}} \quad \text{on} \quad \partial\Omega_2. \tag{2.1c}$$

In (2.1a), the harmonic function u may represent an electric potential in electrostatics or a temperature in steady–state heat conduction. Also, the Dirichlet BC (2.1c) may be replaced by a Robin BC to model the heat exchange with the surrounding environment. The domains Ω_1 and Ω_2 are bounded with sufficiently smooth boundaries $\partial\Omega_1$ and $\partial\Omega_2$, the perfectly conducting rigid inclusion Ω_1 is compactly contained in Ω_2 and $\Omega = \Omega_2 \backslash \overline{\Omega}_1$ is assumed connected. The temperature u_{ext} in (2.1c) along the exposed boundary $\partial\Omega_2$ may be experimentally measured with an infrared scanner. The BC (2.1b) models the presence of the rigid inclusion Ω_1 on whose boundary it is applied, where u_{int} is a constant (usually equal to zero as one can work with $u - u_{\text{int}}$), which may be known or unknown. In the latter case, we need to also impose an extra condition $\int_{\partial\Omega_2} \frac{\partial u}{\partial n} ds = 0$, see [10], where $\boldsymbol{n}$ is the outward unit normal to the boundary $\partial\Omega_2$. In this paper, we assume for simplicity, that the constant u_{int} in (2.1b) is known.

As in the inverse problem Ω_1 is unknown, to compensate for this missing information, we consider the additional measured internal data

$$u(\mathbf{x}_\ell) = u_\ell \quad \text{at the points} \quad (\mathbf{x}_\ell)_{\ell=\overline{1,L}} \in \Omega. \tag{2.1d}$$

Alternatively, one could measure the flux $\partial_n u$ on a portion of $\partial\Omega_2$, where $\boldsymbol{n}$ is the outward unit normal to the boundary $\partial\Omega_2$, as in electrical impedance tomography [6].

The internal measurements in (2.1d) are understood to have been taken with sensors (thermocouples) embedded within the material prior to any practical installation and have also been considered previously in inverse Cauchy steady–state heat conduction problems [14]. Of course, in order to achieve the uniqueness of solution, the measurement points $\mathbf{x}_\ell \in \Omega$ for $\ell = \overline{1, L}$, (with L reasonably large) should be spread (preferably uniformly) on a fixed prescribed closed, non–intersecting curve $\partial\Omega_4$ such that the unknown void Ω_1 is always a subset of Ω_4. This would then ensure that the direct Dirichlet problem for the Laplace equation in the annulus $\Omega_2 \backslash \Omega_4$ can be solved to provide the Neumann data on the inner boundary $\partial\Omega_4$. Then, on the boundary $\partial\Omega_4$, we would have available the Cauchy data which secures the unique identification of the rigid inclusion Ω_1, see e.g., [10, 22]. As for the existence of solution of the inverse problem (2.1a)–(2.1d), it is assumed that the extra measured data (2.1d) is compatible, i.e. it arises from the solution of the direct well–posed problem (2.1a)–(2.1c), see [4] for more discussion on the issue of compatibility of Cauchy data in inverse problems.

3. The method of fundamental solutions (MFS)

In the MFS, we represent a harmonic function satisfying the Laplace equation (2.1a) as a linear combination of $2N$ *non–singular* fundamental solutions

$$u_N(\boldsymbol{c}, \boldsymbol{\xi}; \boldsymbol{x}) = \sum_{k=1}^{2N} c_k \, G(\boldsymbol{x}, \boldsymbol{\xi}_k), \quad \boldsymbol{x} \in \overline{\Omega}, \tag{3.1}$$

where G is the fundamental solution of the Laplace operator, given by

$$G(\boldsymbol{x}, \boldsymbol{\xi}) = \begin{cases} -\dfrac{1}{2\pi} \, \ln |\boldsymbol{x} - \boldsymbol{\xi}| \ \text{ in 2D}, \\ \\ \dfrac{1}{4\pi} \, \dfrac{1}{|\boldsymbol{x} - \boldsymbol{\xi}|} \ \text{ in 3D}, \end{cases} \tag{3.2}$$

and the source points $\boldsymbol{\xi}_k$ are situated outside $\overline{\Omega}$. The justification for the expansion (3.1) is given by the denseness of the set of single–layer potentials, involving the fundamental solutions (3.2) with sources located outside $\overline{\Omega}$, into the set of harmonic functions in Ω, [1, 5].

We shall follow the steps in the approach described in [27]. Note that although the description provided in the sequel is for inverse geometric problems in 2D, it can be easily extended to corresponding problems in 3D, as indeed will be later shown in section 5.2 in the context of 3D linear elasticity.

3.1. **Step 1: Direct problem.** The first step is to devise or select a suitable direct problem solver that is fast and accurate to be used iteratively (or non–iteratively) in a minimization process required when solving inverse problems. The direct problem solver is also needed to fabricate the numerically simulated extra data (2.1c) in cases when an analytical solution to the direct problem (2.1a)–(2.1c) is not available. Moreover, in Step 1, the direct problem methodology yields, through the linear system of equations (3.10) derived below, an explicit discrete representation of the direct map connecting the set of MFS unknown coefficients $\boldsymbol{c} = (c_k)_{k=\overline{1,2N}}$ to the finite set of L internal measurements (2.1c). We therefore consider the direct BVP consisting of (2.1a)–(2.1c) with the boundary $\partial\Omega_1$ known. In this formulation, a total of $2N$ sources $(\boldsymbol{\xi}_k)_{k=\overline{1,2N}}$ are placed outside the domain $\overline{\Omega}$, i.e. in $\Omega_1 \cup \left(\mathbb{R}^2 \backslash \overline{\Omega}_2\right)$. The first N of these sources, $(\boldsymbol{\xi}_k)_{k=\overline{1,N}}$, are placed in Ω_1, on a pseudo–boundary $\partial\Omega_1'$ similar to $\partial\Omega_1$. The remaining N sources $(\boldsymbol{\xi}_k)_{k=\overline{N+1,2N}}$ are placed in $\mathbb{R}^2 \backslash \overline{\Omega}_2$, on a pseudo–boundary $\partial\Omega_2'$ similar to $\partial\Omega_2$. In the current MFS approach the two pseudo–boundaries $\partial\Omega_1'$ and $\partial\Omega_2'$ are fixed.

We shall take the exterior boundary $\partial\Omega_2$ to be a circle of radius R centred at the origin, hence the sources on $\partial\Omega_2'$ will be

$$\boldsymbol{\xi}_{N+k} = \zeta_{\text{ext}}\, R\,(\cos\vartheta_k, \sin\vartheta_k), \quad \vartheta_k = \frac{2\pi(k-1)}{N}, \quad k = \overline{1,N}, \tag{3.3}$$

and the known dilation parameter $\zeta_{\text{ext}} > 1$. For simplicity, let us assume that the boundary $\partial\Omega_1$ is a smooth, star–like curve with respect to the origin. Then, in polar coordinates the equation of $\partial\Omega_1$ is

$$x = r(\vartheta)\,\cos\vartheta, \qquad y = r(\vartheta)\,\sin\vartheta, \qquad \vartheta \in [0, 2\pi), \tag{3.4}$$

where r is a smooth $2\pi-$periodic function. The source points on $\partial\Omega_1'$ will be

$$\boldsymbol{\xi}_k = \zeta_{\text{int}}\, r(\vartheta_k)\,(\cos\vartheta_k, \sin\vartheta_k)\,, \quad k = \overline{1,N}, \tag{3.5}$$

where $\zeta_{\text{int}} \in (0,1)$ is the contraction parameter. In addition to the sources we shall also define $2M$ boundary collocation points. The first M of these, $(\boldsymbol{x}_k)_{k=\overline{1,M}}$ will be placed on $\partial\Omega_1$, as follows:

$$\boldsymbol{x}_k = r(\tilde{\vartheta}_k)\,\left(\cos\tilde{\vartheta}_k, \sin\tilde{\vartheta}_k\right), \quad k = \overline{1,M}, \tag{3.6}$$

where $\tilde{\vartheta}_k = 2\pi(k-1)/M,\ k = \overline{1,M}$. The remaining M points $(\boldsymbol{x}_{M+k})_{k=\overline{1,M}}$ will be placed on $\partial\Omega_2$, i.e.

$$\boldsymbol{x}_{M+k} = R\,(\cos\tilde{\vartheta}_k, \sin\tilde{\vartheta}_k), \quad k = \overline{1,M}. \tag{3.7}$$

The pseudo–boundaries on which the sources are placed and the domain of this BVP are presented in Figure 1(a).

Collocation of the BCs (2.1b)–(2.1c) at the $2M$ boundary collocation points (3.6)–(3.7), via (3.1), leads to the linear system of equations

$$A\,\boldsymbol{c} = \boldsymbol{u}, \tag{3.8}$$

where the matrix $A \in \mathbb{R}^{2M\times 2N}$ is defined by

$$A_{i,j} = G(\boldsymbol{x}_i, \boldsymbol{\xi}_j), \quad i = \overline{1,2M},\ j = \overline{1,2N},$$

$\boldsymbol{u} \in \mathbb{R}^{2M\times 1}$ is defined by

$$u_i = u_{\rm int}, \quad u_{M+i} = u_{\rm ext}(\boldsymbol{x}_{M+i}), \quad i = \overline{1, M},$$

and $\boldsymbol{c} \in \mathbb{R}^{2N\times 1}$ is the vector of unknown coefficients. Having determined $\boldsymbol{c}$ by solving the system of equations (3.8) we calculate the approximation (3.1) at the additional points (2.1d) to yield

$$u_N(\boldsymbol{c}, \boldsymbol{\xi}; \mathbf{x}_\ell) = \sum_{k=1}^{2N} c_k\, G(\mathbf{x}_\ell, \boldsymbol{\xi}_k), \quad \ell = \overline{1, L}. \tag{3.9}$$

If we define the vector $\boldsymbol{u}_{\rm meas} = [u_N(\boldsymbol{c}, \boldsymbol{\xi}; \mathbf{x}_1), u_N(\boldsymbol{c}, \boldsymbol{\xi}; \mathbf{x}_2), \ldots, u_N(\boldsymbol{c}, \boldsymbol{\xi}; \mathbf{x}_L)]^T$, the system of equations (3.9) can be written as

$$\boldsymbol{u}_{\rm meas} = B\, \boldsymbol{c}, \tag{3.10}$$

where $B \in \mathbb{R}^{L\times 2N}$ is given by

$$B_{\ell,j} = G(\mathbf{x}_\ell, \boldsymbol{\xi}_j), \quad \ell = \overline{1, L},\ j = \overline{1, 2N}.$$

3.2. **Step 2: Inverse problem.** In the inverse problem, equations (3.8) and (3.10) can be assembled as a nonlinear system of algebraic equations in the unknowns consisting of the coefficients $\boldsymbol{c} = (c_k)_{k=\overline{1,2N}}$ and the radii $\boldsymbol{r} = (r(\tilde{\theta}_i)_{i=\overline{1,M}}$, which can be solved using a nonlinear least–squares method penalised with extra regularization to achieve a stable solution. However, if we analyse the BVP (2.1a)–(2.1c) again, but instead of the boundary $\partial\Omega_1$ we consider the known circular virtual boundary $\partial\Omega_3$ with radius r_0 centred at the origin, such that $0 < r_0 < R$, so now $\Omega := \Omega_2 \backslash \overline{\Omega}_3$, see Figure 1(b), it is possible to obtain the vector $\boldsymbol{c}$ of MFS coefficients separately using only matrix/vector linear algebra manipulations, as follows. We select $\mathcal{N}$ sources as in (3.3) given by

$$\boldsymbol{\xi}_{\mathcal{N}+k} = \eta_{\rm ext}\, R\, (\cos\varphi_k, \sin\varphi_k)\,, \quad k = \overline{1, \mathcal{N}}, \tag{3.11}$$

where $\varphi_k = 2\pi(k-1)/\mathcal{N}$ for $k = \overline{1, \mathcal{N}}$, and for the remaining $\mathcal{N}$ sources, instead of (3.5), we take

$$\boldsymbol{\xi}_k = \eta_{\rm int}\, r_0\, (\cos\varphi_k, \sin\varphi_k)\,, \quad k = \overline{1, \mathcal{N}}, \tag{3.12}$$

where $\eta_{\rm int} \in (0, 1)$. We also select $2\mathcal{N}$ collocation points as

$$\partial\Omega_3 \ni\ \boldsymbol{x}_k = r_0\, (\cos\varphi_k, \sin\varphi_k)\,, \quad k = \overline{1, \mathcal{N}}, \tag{3.13}$$

and

$$\partial\Omega_2 \ni\ \boldsymbol{x}_{\mathcal{N}+k} = R\,(\cos\varphi_k, \sin\varphi_k), \quad k = \overline{1, \mathcal{N}}. \tag{3.14}$$

A depiction of the features of this BVP is shown in Figure 1(b). Following [27], collocating the approximation (3.1) at the $2\mathcal{N}$ collocation points (3.13) and (3.14) leads to the system of equations (3.8), where now the matrix $A \in \mathbb{R}^{2\mathcal{N}\times 2\mathcal{N}}$ is square and defined by

$$A_{i,j} = G(\boldsymbol{x}_i, \boldsymbol{\xi}_j), \quad i, j = \overline{1, 2\mathcal{N}}, \tag{3.15}$$

$\boldsymbol{u} \in \mathbb{R}^{2\mathcal{N}\times 1}$ is defined by

$$u_i = u_{{\rm vir}_i}, \quad u_{\mathcal{N}+i} = u_{\rm ext}(\boldsymbol{x}_{\mathcal{N}+i}), \quad i = \overline{1, \mathcal{N}},$$

and $\boldsymbol{c} \in \mathbb{R}^{2\mathcal{N}\times 1}$ is the vector of unknown coefficients. Note that the values $(u_{\text{vir}_i})_{i=\overline{1,\mathcal{N}}}$ are also unknown. Moreover, the matrix B in (3.10) is now defined by

$$B_{\ell,j} = G(\mathbf{x}_\ell, \boldsymbol{\xi}_j), \quad \ell = \overline{1,L},\ j = \overline{1,2\mathcal{N}}. \tag{3.16}$$

From (3.8), with the current definitions of A and $\boldsymbol{u}$, we may write

$$\boldsymbol{c} = A^{-1}\boldsymbol{u} = A^{-1}\left[\begin{array}{c}\boldsymbol{u}_\alpha\\ \hline \boldsymbol{u}_\beta\end{array}\right], \tag{3.17}$$

where $\boldsymbol{u}_\alpha = [u_{\text{vir}_1}, u_{\text{vir}_2}, \ldots, u_{\text{vir}_\mathcal{N}}]^T$ and $\boldsymbol{u}_\beta = [u_{\text{ext}}(\boldsymbol{x}_{\mathcal{N}+1}), u_{\text{ext}}(\boldsymbol{x}_{\mathcal{N}+2}), \ldots, u_{\text{ext}}(\boldsymbol{x}_{2\mathcal{N}})]^T$. Note that the vector $\boldsymbol{u}_\alpha$ is unknown. Also, from (3.10) and (3.17) we may denote (with the current definitions of matrices A and B in (3.15) and (3.16), respectively)

$$\tilde{\boldsymbol{u}}_{\text{meas}} := B\,\boldsymbol{c} = BA^{-1}\boldsymbol{u} = [A_1|A_2]\left[\begin{array}{c}\boldsymbol{u}_\alpha\\ \hline \boldsymbol{u}_\beta\end{array}\right] = A_1\boldsymbol{u}_\alpha + A_2\boldsymbol{u}_\beta = A_1\boldsymbol{u}_\alpha + \boldsymbol{g}, \tag{3.18}$$

where $[A_1|A_2] = BA^{-1}$ with $A_1, A_2 \in \mathbb{R}^{L\times\mathcal{N}}$ and $\boldsymbol{g} = A_2\boldsymbol{u}_\beta$. Note that $\boldsymbol{g} \in \mathbb{R}^{L\times 1}$ is known.

We seek to minimize the difference between the measurement vector $\boldsymbol{u}_{\text{meas}}$ and the estimate of the measurement vector $\tilde{\boldsymbol{u}}_{\text{meas}}$ in (3.18) by minimizing the multivariate error function

$$E(\boldsymbol{u}_\alpha) = (\tilde{\boldsymbol{u}}_{\text{meas}} - \boldsymbol{u}_{\text{meas}})^T(\tilde{\boldsymbol{u}}_{\text{meas}} - \boldsymbol{u}_{\text{meas}}) \tag{3.19}$$

or, from (3.18),

$$E(\boldsymbol{u}_\alpha) = (\boldsymbol{u}_\alpha^T A_1^T + \boldsymbol{g}^T - \boldsymbol{u}_{\text{meas}}^T)(A_1\boldsymbol{u}_\alpha + \boldsymbol{g} - \boldsymbol{u}_{\text{meas}}). \tag{3.20}$$

To obtain the optimal $\boldsymbol{u}_\alpha$ for minimizing E we solve

$$\nabla_{\boldsymbol{u}_\alpha} E(\boldsymbol{u}_\alpha) = 2A_1^T A_1\boldsymbol{u}_\alpha + 2A_1^T(\boldsymbol{g} - \boldsymbol{u}_{\text{meas}}) = \mathbf{0} \tag{3.21}$$

to result in

$$\boldsymbol{u}_\alpha = \left(A_1^T A_1\right)^\dagger A_1^T(\boldsymbol{u}_{\text{meas}} - \boldsymbol{g}). \tag{3.22}$$

The solution (3.22) is introduced into (3.17) to obtain the vector of coefficients $\boldsymbol{c} = (c_j)_{j=\overline{1,2\mathcal{N}}}$ and to finally obtain the approximation

$$u_\mathcal{N}(\boldsymbol{c}, \boldsymbol{\xi}; \boldsymbol{x}) = \sum_{k=1}^{2\mathcal{N}} c_k\, G(\boldsymbol{x}, \boldsymbol{\xi}_k), \quad \boldsymbol{x} \in \Omega_2\backslash\overline{\Omega_3} \tag{3.23}$$

to the solution of BVP (2.1a)–(2.1c) in the domain $\Omega_2\backslash\overline{\Omega_3}$.

Remark. In (3.22), the matrix $A_1^T A_1 \in \mathbb{R}^{\mathcal{N}\times\mathcal{N}}$ is poorly conditioned if $L \geq \mathcal{N}$ or singular if $L < \mathcal{N}$, and its Moore–Penrose pseudoinverse $\left(A_1^T A_1\right)^\dagger$ is calculated with the MATLAB® function `pinv(`$A_1^T A_1$`,tol)`. This function is based on the SVD of the matrix $A_1^T A_1$. More specifically, the SVD takes the form

$$A_1^T\, A_1 = U\,\Sigma\, V^T, \tag{3.24}$$

where $\Sigma = \text{diag}\,(\sigma_1, \sigma_2, \ldots, \sigma_\mathcal{N}) \in \mathbb{R}^{\mathcal{N}\times\mathcal{N}}$ is a diagonal matrix with its singular values satisfying

$$\sigma_1 \geq \sigma_2 \geq \ldots \geq \sigma_\mathcal{N} \geq 0.$$

In order to deal with the ill–conditioning of the matrix in (3.24), in `pinv`, singular values which are smaller than the specified singular value tolerance `tol` are treated as zero, in which case, instead of (3.24) we can write

$$A_1^T A_1 = [U_1\, U_2] \begin{bmatrix} \Sigma_1 & 0 \\ 0 & 0 \end{bmatrix} [V_1\, V_2]^T \,, \tag{3.25}$$

where $\Sigma_1 = \text{diag}\,(\sigma_1, \sigma_2, \ldots, \sigma_{\mathcal{N}_1})$ is an $\mathcal{N}_1 \times \mathcal{N}_1$ diagonal matrix and, $\sigma_\ell < \texttt{tol}$, $\ell = \mathcal{N}_1 + 1, \ldots, \mathcal{N}$. The Moore–Penrose pseudoinverse of $A_1^T A_1$ is then

$$\left(A_1^T A_1\right)^\dagger = V_1\, \Sigma_1^{-1}\, U_1^T. \tag{3.26}$$

This is the essence of truncated SVD [11], see also [12, Section 4.2], which is a spectral filtering method removing small singular values and providing regularization if `tol` is selected appropriately depending on the amount of noise with which the measured data (2.1d) is contaminated.

3.3. **Step 3.** Assuming that u can be analytically continued in $\Omega_2 \backslash \overline{\Omega}_3$, [24], we solve the BVP in the virtual domain $\Omega_2 \backslash \overline{\Omega}_3$ with the known boundary data (2.1c) on $\partial\Omega_2$ and the calculated data $\boldsymbol{u}_\alpha$ on $\partial\Omega_3$ given by (3.22), and evaluate $u_{\mathcal{N}}$. More specifically, assuming that $\Omega_3 \subset \Omega_1 \subset \Omega_4$, we then seek the level–set iso–curve or iso–surface $u_{\mathcal{N}} = u_{\text{int}} \equiv$ constant to determine the boundary $\partial\Omega_1$ of the unknown rigid inclusion Ω_1. This task is accomplished via the MATLAB® functions `contour` in 2D and `isosurface` in 3D. We can then seek for the boundary $\partial\Omega_1$ of the rigid inclusion as the level-set of a curve/surface satisfying (2.1b), [13].

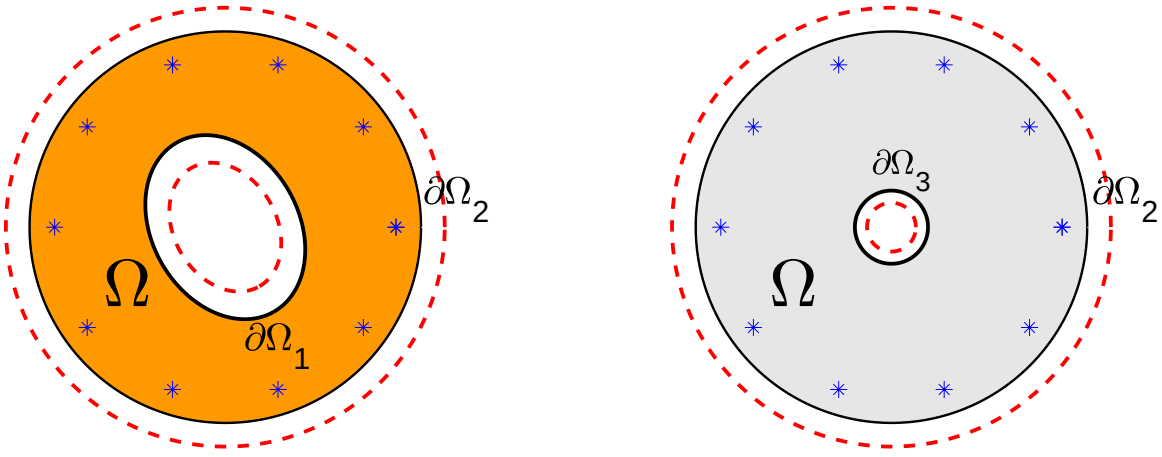

(a) Step 1 (b) Steps 2-3

FIGURE 1. Problem discretization: (a) Geometry of direct problem in Step 1, (b) Geometry of inverse problem in Steps 2–3. The pseudo–boundaries are denoted by dotted red curves (- -) and the measurement points by blue asterisks (*).

4. Numerical examples

To avoid an inverse crime, we took different numbers of degrees of freedom in the solutions of the direct (M, N) and inverse $(\mathcal{N})$ problems. We also choose values for ζ_{int}, ζ_{ext} which are, respectively, different to η_{int}, η_{ext}. The calculated measured data (3.10) in Step 1 were contaminated with noise by replacing $(\boldsymbol{u}_{\text{meas}})_m$ by $(1+p\,\varrho_m)(\boldsymbol{u}_{\text{meas}})_m$, $m=\overline{1,L}$, where p is the percentage noise added and $[\varrho_1, \varrho_2, \ldots, \varrho_L]^T$ is a random noisy variable vector in [-1,1] obtained via the MATLAB® command `-1+2*rand(1,L)`. Unless otherwise stated, all shapes considered are centred at the origin of the Cartesian coordinates system. The boundary values in (2.1b) and (2.1c) are taken as $u_{\text{int}} = 1$ and $u_{\text{ext}} = 10$ in Examples 1–6. In the 2D Examples 1–5, the exterior circle $\partial\Omega_2$ has a radius $R = 1$ and the virtual circle $\partial\Omega_3$ has radius 0.3 (in Examples 1–4) and 0.25 (in Example 5). In the 2D examples we also select $L = 10$ points for Examples 1–3, $L = 15$ for Example 4 and $L = 20$ for Example 5 on the circle $\partial\Omega_4$ with radius 0.85 for the measurement points in (2.1d). In Step 1, we solved the direct problem in Examples 1–5 with $M = N = 20$ and in Steps 2 and 3 we took $\mathcal{N} = 25$. Finally, unless otherwise stated, in Step 3 the solution was evaluated on a 41×41 polar grid in the virtual domain $\Omega_2 \backslash \overline{\Omega}_3$ in order to impose (2.1b) and determine the boundary $\partial\Omega_1$ of the inclusion Ω_1. In Figures 2–6, the reconstructed curve is in red, the virtual circle $\partial\Omega_3$ in blue, the outer circle $\partial\Omega_2$ in black, the true curve $\partial\Omega_1$ in black dots and the measurement points on $\partial\Omega_4$ in blue asterisks.

4.1. **Example 1.** We consider Example 1 from [27] where the curve to be reproduced is a circle of radius 0.5. In Figure 2 we present the reconstructed results obtained with no noise and noise $p = 5\%$ and various values of `tol`, which are shown to improve the reconstructed curve. In case of no noise, the use of `tol` was not found necessary and all singular values were taken into account in (3.25). However, when the input data (2.1d) is contaminated with noise, since the inverse problem is ill–posed by violating the continuous dependence on the input data, the use of the regularization parameter `tol` is necessary in order to obtain a stable and meaningful recovery of the unknown rigid inclusion Ω_1. For instance, Figure 2(b) shows that if `tol` is not chosen appropriately then the recovered contour of $\partial\Omega_1$ satisfying $u_{\mathcal{N}} = u_{\text{int}}$ is not physically meaningful, being clearly unstable. However, appropriate choices of `tol`, such as in Figure 2(c) and even better in Figure 2(d), reveal that a stable and meaningful solution can be achieved with the proposed method. Note that in the interest of open science and reproducibility the MATLAB® code for this example is available at [29].

In the next two examples we assess the performance of the method for reconstructing more complicated elliptical– or sinusoidal–shape rigid inclusions.

4.2. **Example 2.** We consider Example 2 from [27] where the curve to be reproduced is an ellipse with a semi–major axis of length 0.7 and a semi–minor one of length 0.5. In Figure 3 we present the reconstructed results obtained with no noise and noise $p = 5\%$ and various values of `tol`, which are shown to improve the reconstructed curve.

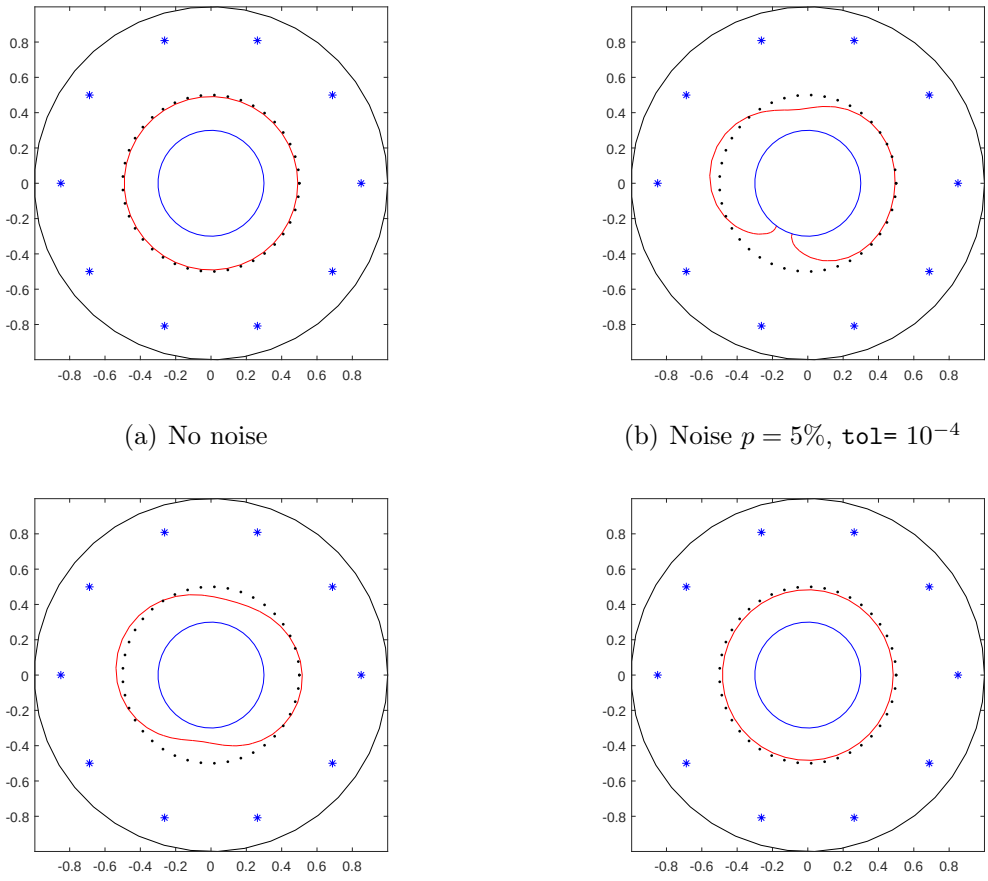

(a) No noise

(b) Noise $p = 5\%$, `tol=` 10^{-4}

(c) Noise $p = 5\%$, `tol=` 10^{-3}

(d) Noise $p = 5\%$, `tol=` 5×10^{-3}

FIGURE 2. Example 1: Reconstruction of boundary $\partial\Omega_1$ with no noise and noise $p = 5\%$ in (2.1d) and various values of `tol`.

4.3. **Example 3.** We next consider Example 3 from [27] where the curve to be reproduced has polar equation $r(\vartheta) = 0.6 + 0.1\sin(\vartheta + \pi/4)$. In Figure 4 we present the reconstructed results obtained with no noise and noise $p = 5\%$ and various values of `tol`, which are shown to improve the reconstructed curve.

In the next two examples we assess the performance of the method in reconstructing more severe concave rigid inclusions having peanut or bean shapes.

4.4. **Example 4.** We next consider a peanut–shaped domain where the curve to be reproduced has polar equation $r(\vartheta) = 0.7\sqrt{\cos^2\vartheta + 0.25\sin^2\vartheta}$. In Figure 5 we present the reconstructed results obtained with no noise and noise $p = 5\%$. For this example, due to the more complex irregular shape, the number of measurements had to be increased from $L = 10$ to $L = 15$ for more

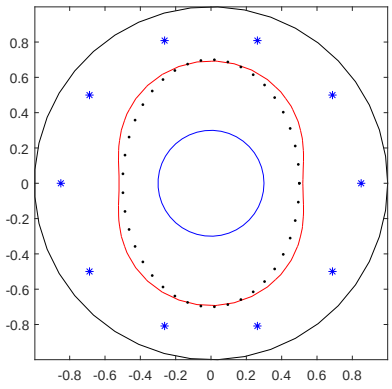

(a) No noise

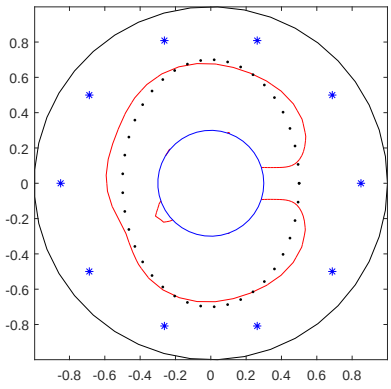

(b) Noise $p = 5\%$, `tol=` 10^{-6}

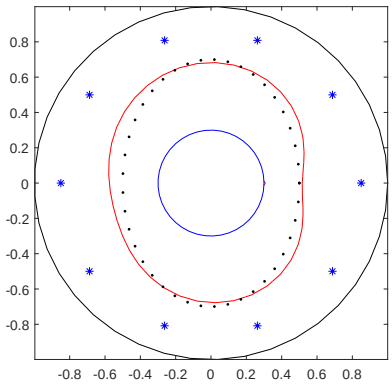

(c) Noise $p = 5\%$, `tol=` 10^{-4}

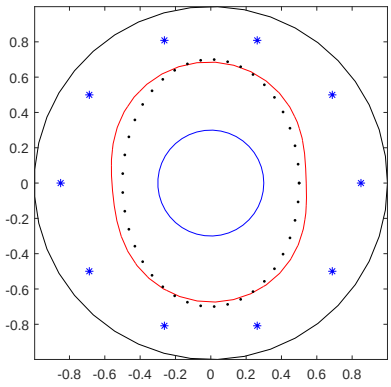

(d) Noise $p = 5\%$, `tol=` 5×10^{-4}

FIGURE 3. Example 2: Reconstruction of boundary with no noise and noise $p = 5\%$ and various values of `tol`.

accurate retrievals. However, the rather unstable recovery presented in Figure 5(b) highlights some limitations of the method to deal with a high level of noise and complicated non–convex rigid inclusions.

4.5. **Example 5.** We next consider a bean-shaped domain where the curve to be reproduced has polar equation $r(\vartheta) = (0.5 + 0.4\cos(\vartheta) + 0.1\sin(2\vartheta))/(1 + 0.7\cos(\vartheta))$. In this case the domain is shifted by (-0.1,0.1). In Figure 6 we present the reconstructed results obtained with no noise and noise $p = 5\%$. As for Example 4, we have increased the number of measurements to $L = 20$ due to the more complex bean–shaped domain Ω_1 to be retrieved. As expected, less accurate and stable reconstructions are obtained compared to the accurate retrievals obtained for the more regular geometries in Examples 1–3.

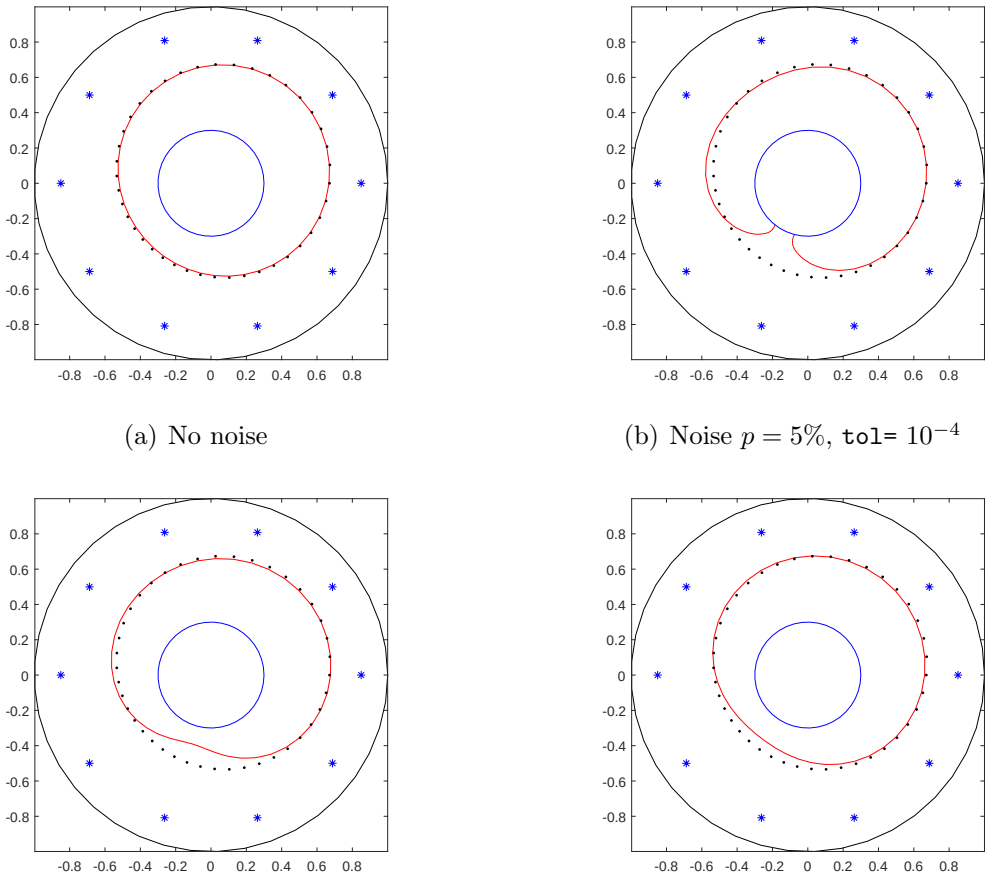

(a) No noise

(b) Noise $p = 5\%$, `tol=` 10^{-4}

(c) Noise $p = 5\%$, `tol=` 10^{-3}

(d) Noise $p = 5\%$, `tol=` 2×10^{-3}

FIGURE 4. Example 3: Reconstruction of boundary with no noise and noise $p = 5\%$ and various values of `tol`.

The next two examples illustrate the capability of the method to reconstruct 3D rigid inclusions.

4.6. **Example 6.** We consider Example 5 from [28], which is a 3D example where the surface to be reproduced is a sphere of radius 0.5. The exterior sphere Ω_2 has radius $R = 1$ and the virtual sphere Ω_3 has radius 0.4. We also select $L = 64$ points on the sphere Ω_4 with radius 0.75 for the measurement points in (2.1d). In Step 1, we solved the direct problem with $M = N = 100$ and in Steps 2 and 3 we took $\mathcal{N} = 144$. Finally, the solution was evaluated in the virtual domain $\Omega_2 \backslash \overline{\Omega}_3$ on a $21 \times 21 \times 21$ spherical grid. In Figure 7 we present the reconstructed results obtained with no noise and noise $p = 5\%$ and various values of `tol`, which are shown to improve the reconstructed curve.

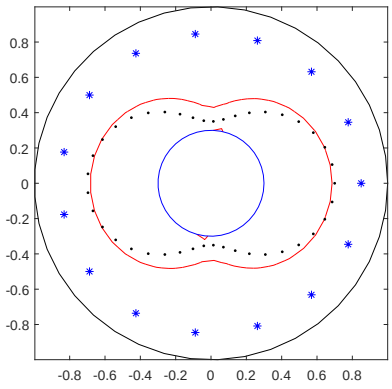

(a) No noise

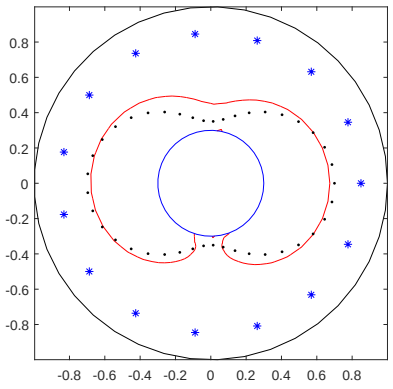

(b) Noise $p = 5\%$, `tol=` 10^{-3}

FIGURE 5. Example 4: Reconstruction of boundary with no noise and noise $p = 5\%$ and various values of `tol`.

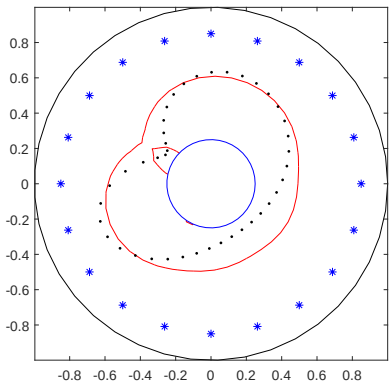

(a) No noise

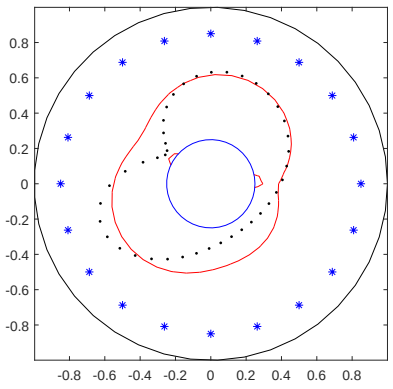

(b) Noise $p = 5\%$, `tol=` 10^{-4}

FIGURE 6. Example 5: Reconstruction of boundary with no noise and noise $p = 5\%$ and various values of `tol`.

4.7. **Example 7.** We consider Example 6 from [28], which is another 3D example. The geometry of the problem is depicted in Figure 8 and consists of a $(0, 0.5) \times (0, 0.5)$ square base and the unknown surface to be reproduced is given by $z = f(x, y) = 0.08 + 0.015 \sin(4\pi x) \cos(4\pi y)$. The BCs on the bottom plane are $u = u_{\text{bottom}} = 10$ and on the top surface $u = u_{\text{top}} = 1$, while on the vertical faces they are $\partial u/\partial n = 0$. The virtual plane is $z = 0.1$ and we select $L = 225$ points on the plane $z = 0.05$ for the measurement points. Note that in this particular problem the description presented in Section 3.2 changes slightly, notably the expression for the matrix A in

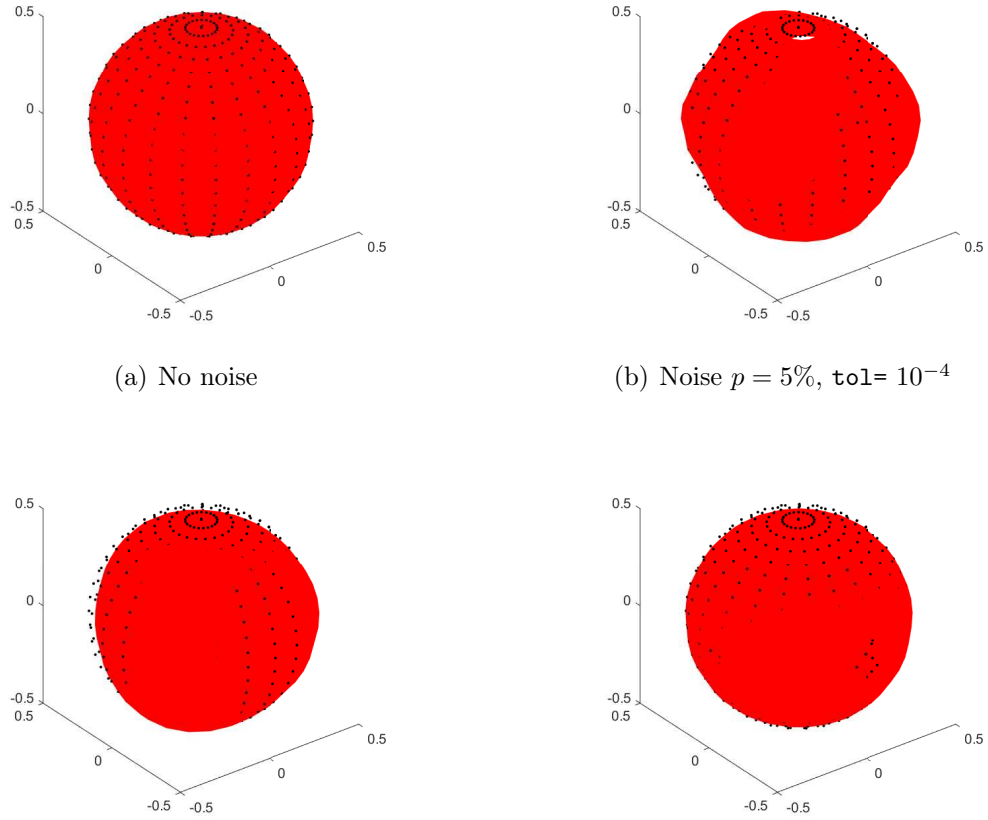

(a) No noise

(b) Noise $p = 5\%$, `tol`= 10^{-4}

(c) Noise $p = 5\%$, `tol`= 10^{-3}

(d) Noise $p = 5\%$, `tol`= 10^{-2}

FIGURE 7. Example 6: Reconstruction of spherical surface with no noise and noise $p = 5\%$ and various values of `tol`.The reproduced surface is in red and the correct curve in black dots.

(3.15) and equations (3.17) and (3.18). In Step 1, we solved the direct problem with 400 points on the top and bottom surface and 100 on the side faces yielding a total of 1200 collocation points and sources. In Steps 2 and 3, we took $\mathcal{N} = 768$. Finally, the solution was evaluated in the virtual domain in a $21 \times 21 \times 21$ grid. In Figure 9 we present the reconstructed results obtained with no noise and noise $p = 5\%$ and various values of `tol`, which are shown to improve the reconstructed curve.

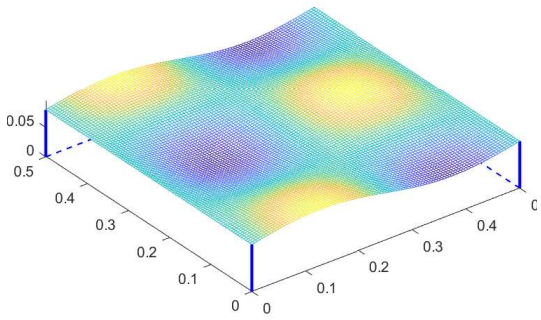

FIGURE 8. Geometry of Example 7.

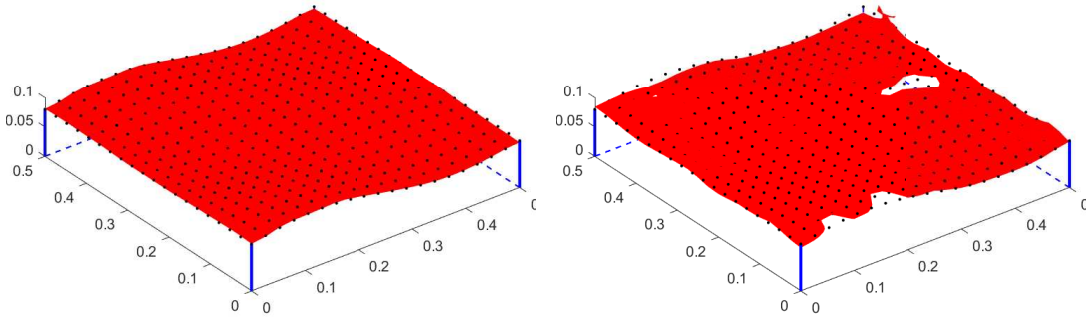

(a) No noise

(b) Noise $p = 5\%$, `tol=` 10^{-4}

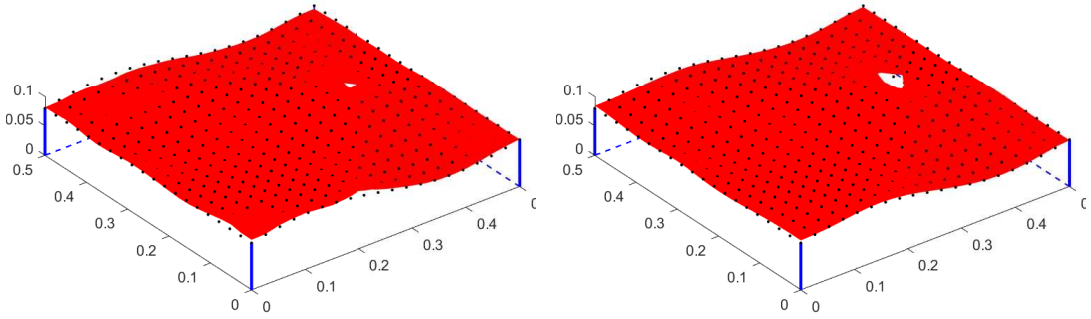

(c) Noise $p = 5\%$, `tol=` 10^{-3}

(d) Noise $p = 5\%$, `tol=` 10^{-2}

FIGURE 9. Example 7: Reconstruction of top surface with no noise and noise $p = 5\%$ and various values of `tol`. The reproduced surface is in red and the correct curve in black dots.

5. Extension to linear elasticity

The analysis of the paper so far has concerned applications to steady–state heat conduction governed by the simple Laplace scalar equation (2.1a). In this section, we formulate the corresponding inverse problems for linear elasticity in both 2D and 3D and describe the development of the non–iterative MFS along with numerical results and discussions.

5.1. **2D problems.**

We first consider the inverse BVP for the Cauchy–Navier equations of linear elasticity in $\mathbb{R}^2$ for the displacement vector $\boldsymbol{u} = (u_1, u_2)$ given by [16]

$$\left(\frac{2-2\nu}{1-2\nu}\right)\frac{\partial^2 u_1}{\partial x^2} + \left(\frac{1}{1-2\nu}\right)\frac{\partial^2 u_2}{\partial x \partial y} + \frac{\partial^2 u_1}{\partial y^2} = 0, \quad \text{in} \quad \Omega = \Omega_2 \backslash \overline{\Omega}_1,$$
$$\frac{\partial^2 u_2}{\partial x^2} + \left(\frac{1}{1-2\nu}\right)\frac{\partial^2 u_1}{\partial x \partial y} + \left(\frac{2-2\nu}{1-2\nu}\right)\frac{\partial^2 u_2}{\partial y^2} = 0, \quad \text{in} \quad \Omega, \tag{5.1a}$$

subject to the Dirichlet BCs

$$u_1 \,=\, u_{\text{int}_1} \equiv \text{constant}, \quad u_2 \,=\, u_{\text{int}_2} \equiv \text{constant} \quad \text{on} \quad \partial\Omega_1 \tag{5.2}$$

and

$$u_1 = u_{\text{ext}_1}, \quad u_2 = u_{\text{ext}_2} \quad \text{on} \quad \partial\Omega_2, \tag{5.3}$$

where $(u_{\text{ext}_1}, u_{\text{ext}_2}) \not\equiv (u_{\text{int}_1}, u_{\text{int}_2})$. In (5.1) $\nu \in (0, 1/2)$ is the Poisson's ratio and the geometry of the BVP is identical to the one described in Section 2. In the inverse problem, the rigid inclusion Ω_1 is unknown and to compensate for it we consider the additional measured internal data of the displacements

$$u_1(\mathbf{x}_\ell) = u_{1_\ell}, \quad u_2(\mathbf{x}_\ell) = u_{2_\ell} \quad \text{at the points} \quad (\mathbf{x}_\ell)_{\ell=\overline{1,L}} \in \Omega. \tag{5.4}$$

As commented at the end of Section 2, if this data is extrapolated to be defined on a closed curve $\partial\Omega_4$ containing the inclusion Ω_1 in its interior, then the uniqueness of the rigid inclusion Ω_1 holds, [2].

In the MFS, we approximate the solution (u_1, u_2) of (5.1) by

$$u_{1_N}(\boldsymbol{c}, \boldsymbol{d}, \boldsymbol{\xi}; \boldsymbol{x}) = \sum_{k=1}^{N} c_k\, G_{11}(\boldsymbol{x}, \boldsymbol{\xi}_k) + \sum_{k=1}^{N} d_k\, G_{12}(\boldsymbol{x}, \boldsymbol{\xi}_k), \quad \boldsymbol{x} \in \overline{\Omega}, \tag{5.5a}$$

$$u_{2_N}(\boldsymbol{c}, \boldsymbol{d}, \boldsymbol{\xi}; \boldsymbol{x}) = \sum_{k=1}^{N} c_k\, G_{21}(\boldsymbol{x}, \boldsymbol{\xi}_k) + \sum_{k=1}^{N} d_k\, G_{22}(\boldsymbol{x}, \boldsymbol{\xi}_k), \quad \boldsymbol{x} \in \overline{\Omega}, \tag{5.5b}$$

where, as in Section 3, $\boldsymbol{\xi}_k$ are the sources located outside $\overline{\Omega}$ and

$$G_{11}(\boldsymbol{x},\boldsymbol{\xi}) = \frac{1}{8\pi\mu(1-\nu)}\left[-(3-4\nu)\ln r + \frac{(x-\xi_x)^2}{r^2}\right], \tag{5.6a}$$

$$G_{12}(\boldsymbol{x},\boldsymbol{\xi}) = \frac{1}{8\pi\mu(1-\nu)}\left[\frac{(x-\xi_x)(y-\xi_y)}{r^2}\right], \tag{5.6b}$$

$$G_{21}(\boldsymbol{x},\boldsymbol{\xi}) = G_{12}(\boldsymbol{x},\boldsymbol{\xi}), \tag{5.6c}$$

$$G_{22}(\boldsymbol{x},\boldsymbol{\xi}) = \frac{1}{8\pi\mu(1-\nu)}\left[-(3-4\nu)\ln r + \frac{(y-\xi_y)^2}{r^2}\right], \tag{5.6d}$$

represent the fundamental solution of the Cauchy–Navier system in 2D. In (5.6), $\boldsymbol{x} = (x, y)$, $\boldsymbol{\xi} = (\xi_x, \xi_y)$, $r = |\boldsymbol{x} - \boldsymbol{\xi}|$ and μ is the shear modulus.
The three steps described in Section 3 are now described as follows.

5.1.1. *Step 1: Direct problem.* We first consider the direct BVP consisting of (5.1)–(5.3) with the boundary $\partial\Omega_1$ known. As in Section 3.1, we take $2N$ sources and $2M$ boundary collocation points and the discretization details are identical.

Collocation of the BCs (5.2)–(5.3) at the $2M$ boundary collocation points leads to a linear system of the form

$$A\begin{pmatrix}\boldsymbol{c}\\ \boldsymbol{d}\end{pmatrix} = \boldsymbol{u}, \tag{5.7}$$

where the matrix $A \in \mathbb{R}^{4M\times 4N}$ has components

$$A_{i,j} = G_{11}(\boldsymbol{x}_i,\boldsymbol{\xi}_j), \quad A_{i,2N+j} = G_{12}(\boldsymbol{x}_i,\boldsymbol{\xi}_j),$$

$$A_{2M+i,j} = G_{21}(\boldsymbol{x}_i,\boldsymbol{\xi}_j), \quad A_{2M+i,2N+j} = G_{22}(\boldsymbol{x}_i,\boldsymbol{\xi}_j), \quad i = \overline{1,2M},\ j = \overline{1,2N},$$

$\boldsymbol{u} \in \mathbb{R}^{4M\times 1}$ has components

$$u_i = u_{\text{int}_1}, \quad u_{M+i} = u_{\text{ext}_1}(\boldsymbol{x}_{M+i}), \quad u_{2M+i} = u_{\text{int}_2}, \quad u_{3M+i} = u_{\text{ext}_2}(\boldsymbol{x}_{M+i}), \qquad i = \overline{1,M},$$

and $\boldsymbol{c}, \boldsymbol{d} \in \mathbb{R}^{2N\times 1}$ are the vectors of unknown coefficients. Having determined $\boldsymbol{c}, \boldsymbol{d}$ by solving the system of equations (5.7), we calculate the approximations (5.5) at the additional points (5.4) from

$$u_{1_N}(\boldsymbol{c},\boldsymbol{d},\boldsymbol{\xi};\mathbf{x}_\ell) = \sum_{k=1}^{N} c_k\, G_{11}(\mathbf{x}_\ell,\boldsymbol{\xi}_k) + \sum_{k=1}^{N} d_k\, G_{12}(\mathbf{x}_\ell,\boldsymbol{\xi}_k), \quad \ell = \overline{1,L}, \tag{5.8}$$

and

$$u_{2_N}(\boldsymbol{c},\boldsymbol{d},\boldsymbol{\xi};\mathbf{x}_\ell) = \sum_{k=1}^{N} c_k\, G_{21}(\mathbf{x}_\ell,\boldsymbol{\xi}_k) + \sum_{k=1}^{N} d_k\, G_{22}(\mathbf{x}_\ell,\boldsymbol{\xi}_k), \quad \ell = \overline{1,L}. \tag{5.9}$$

If we define the vector

$$\boldsymbol{u}_{\text{meas}} = \left[u_{1_N}(\boldsymbol{c},\boldsymbol{\xi};\mathbf{x}_1, u_{1_N}(\boldsymbol{c},\boldsymbol{\xi};\mathbf{x}_2), \ldots, u_{1_N}(\boldsymbol{c},\boldsymbol{\xi};\mathbf{x}_L), u_{2_N}(\boldsymbol{c},\boldsymbol{\xi};\mathbf{x}_1), u_{2_N}(\boldsymbol{c},\boldsymbol{\xi};\mathbf{x}_2), \ldots, u_{2_N}(\boldsymbol{c},\boldsymbol{\xi};\mathbf{x}_L)\right]^T,$$

equations (5.8) and (5.9) can be combined as

$$\boldsymbol{u}_{\text{meas}} = B\left(\frac{\boldsymbol{c}}{\boldsymbol{d}}\right), \tag{5.10}$$

where the matrix $B \in \mathbb{R}^{2L\times 4N}$ has the components

$$B_{\ell,j} = G_{11}(\mathbf{x}_\ell, \boldsymbol{\xi}_j), \quad B_{\ell,2N+j} = G_{12}(\mathbf{x}_\ell, \boldsymbol{\xi}_j),$$

$$B_{L+\ell,j} = G_{21}(\mathbf{x}_\ell, \boldsymbol{\xi}_j), \quad B_{L+\ell,2N+j} = G_{22}(\mathbf{x}_\ell, \boldsymbol{\xi}_j), \quad \ell = \overline{1,L},\ j = \overline{1,2N}.$$

5.1.2. *Step 2: Inverse problem.* As in Section 3.2, we examine the BVP (5.1)–(5.3) again but instead of the boundary $\partial\Omega_1$ we consider the known circular virtual boundary $\partial\Omega_3$ with radius $r_0 > 0$ centred at the origin, see Figure 1(b).
Collocating the approximation (3.1) at the $2\mathcal{N}$ collocation points leads to a system of equations (5.7), where now the matrix $A \in \mathbb{R}^{4\mathcal{N}\times 4\mathcal{N}}$ is square and defined by

$$A_{i,j} = G_{11}(\boldsymbol{x}_i, \boldsymbol{\xi}_j), \quad A_{i,2\mathcal{N}+j} = G_{12}(\boldsymbol{x}_i, \boldsymbol{\xi}_j),$$

$$A_{2\mathcal{N}+i,j} = G_{21}(\boldsymbol{x}_i, \boldsymbol{\xi}_j), \quad A_{2\mathcal{N}+i,2\mathcal{N}+j} = G_{22}(\boldsymbol{x}_i, \boldsymbol{\xi}_j), \quad i,j = \overline{1,2\mathcal{N}}, \tag{5.11}$$

$\boldsymbol{u} \in \mathbb{R}^{4\mathcal{N}\times 1}$ is defined by

$$u_i = u_{\text{vir}_{1_i}}, \quad u_{\mathcal{N}+i} = u_{\text{ext}_1}(\boldsymbol{x}_{\mathcal{N}+i}), \quad u_{2\mathcal{N}+i} = u_{\text{vir}_{2_i}}, \quad u_{3\mathcal{N}+i} = u_{\text{ext}_2}(\boldsymbol{x}_{\mathcal{N}+i}), \quad i = \overline{1,\mathcal{N}},$$

and $\boldsymbol{c}, \boldsymbol{d} \in \mathbb{R}^{2\mathcal{N}\times 1}$ are the vectors of unknown coefficients. Note that the values $\left(u_{\text{vir}_{1_i}}\right)_{i=\overline{1,\mathcal{N}}}$ and $\left(u_{\text{vir}_{2_i}}\right)_{i=\overline{1,\mathcal{N}}}$ are also unknown. Moreover, the matrix B in (5.10) is now defined by

$$B_{\ell,j} = G_{11}(\mathbf{x}_\ell, \boldsymbol{\xi}_j), \quad B_{\ell,2\mathcal{N}+j} = G_{12}(\mathbf{x}_\ell, \boldsymbol{\xi}_j),$$

$$B_{L+\ell,j} = G_{21}(\mathbf{x}_\ell, \boldsymbol{\xi}_j), \quad B_{L+\ell,2\mathcal{N}+j} = G_{22}(\mathbf{x}_\ell, \boldsymbol{\xi}_j), \quad \ell = \overline{1,L},\ j = \overline{1,2\mathcal{N}}. \tag{5.12}$$

From (5.7), with the current definitions of A and $\boldsymbol{u}$, we may write

$$\left(\frac{\boldsymbol{c}}{\boldsymbol{d}}\right) = A^{-1}\boldsymbol{u} = A^{-1}\left[\begin{array}{c} \boldsymbol{u}_\alpha \\ \hline \boldsymbol{u}_\beta \\ \hline \boldsymbol{u}_\gamma \\ \hline \boldsymbol{u}_\delta \end{array}\right], \tag{5.13}$$

where

$$\boldsymbol{u}_\alpha = \left[u_{\text{vir}_{1_1}}, u_{\text{vir}_{1_2}}, \ldots, u_{\text{vir}_{1_\mathcal{N}}}\right]^T, \quad \boldsymbol{u}_\beta = \left[u_{\text{ext}_1}(\boldsymbol{x}_{\mathcal{N}+1}), u_{\text{ext}_1}(\boldsymbol{x}_{\mathcal{N}+2}), \ldots, u_{\text{ext}_1}(\boldsymbol{x}_{2\mathcal{N}})\right]^T,$$

$$\boldsymbol{u}_\gamma = \left[u_{\text{vir}_{2_1}}, u_{\text{vir}_{2_2}}, \ldots, u_{\text{vir}_{2_\mathcal{N}}}\right]^T, \quad \boldsymbol{u}_\delta = \left[u_{\text{ext}_2}(\boldsymbol{x}_{\mathcal{N}+1}), u_{\text{ext}_2}(\boldsymbol{x}_{\mathcal{N}+2}), \ldots, u_{\text{ext}_2}(\boldsymbol{x}_{2\mathcal{N}})\right]^T.$$

Note that the vectors $\boldsymbol{u}_\alpha$ and $\boldsymbol{u}_\gamma$ are unknown.

Also, from (5.10) and (5.13) we may write (with the current definitions of matrices A and B in (5.11) and (5.12), respectively)

$$\tilde{\boldsymbol{u}}_{\text{meas}} = B\,\boldsymbol{c} = BA^{-1}\boldsymbol{u} = [A_1|A_2|A_3|A_4]\left[\begin{array}{c}\boldsymbol{u}_\alpha\\ \hline \boldsymbol{u}_\beta\\ \hline \boldsymbol{u}_\gamma\\ \hline \boldsymbol{u}_\delta\end{array}\right] = A_1\boldsymbol{u}_\alpha + A_2\boldsymbol{u}_\beta + A_3\boldsymbol{u}_\gamma + A_4\boldsymbol{u}_\delta = A_{13}\boldsymbol{v} + \boldsymbol{g}, \quad (5.14)$$

where $[A_1|A_2|A_3|A_4] = BA^{-1}$ with $A_1, A_2, A_3, A_4 \in \mathbb{R}^{2L\times\mathcal{N}}$, $A_{13} = [A_1|A_3]$, $\boldsymbol{g} = A_2\boldsymbol{u}_\beta + A_4\boldsymbol{u}_\delta$, and

$$\boldsymbol{v} = \left(\begin{array}{c}\boldsymbol{u}_\alpha\\ \hline \boldsymbol{u}_\gamma\end{array}\right).$$

Note that $\boldsymbol{g} \in \mathbb{R}^{2L\times 1}$ is known.
We seek to minimize the difference between the measurement vector $\boldsymbol{u}_{\text{meas}}$ and the estimate of the measurement vector $\tilde{\boldsymbol{u}}_{\text{meas}}$ in (5.14) by examining the multivariate error function

$$E(\boldsymbol{v}) = (\tilde{\boldsymbol{u}}_{\text{meas}} - \boldsymbol{u}_{\text{meas}})^T(\tilde{\boldsymbol{u}}_{\text{meas}} - \boldsymbol{u}_{\text{meas}}) \quad (5.15)$$

or, from (3.18),

$$E(\boldsymbol{v}) = (\boldsymbol{v}^T A_{13}^T + \boldsymbol{g}^T - \boldsymbol{u}_{\text{meas}}^T)(A_{13}\boldsymbol{v} + \boldsymbol{g} - \boldsymbol{u}_{\text{meas}}). \quad (5.16)$$

To obtain the optimal $\boldsymbol{v}$ for minimizing E we take

$$\nabla_{\boldsymbol{v}} E(\boldsymbol{v}) = 2A_{13}^T A_{13}\boldsymbol{v} + 2A_{13}^T(\boldsymbol{g} - \boldsymbol{u}_{\text{meas}}) = \boldsymbol{0} \quad (5.17)$$

or

$$\boldsymbol{v} = \left(A_{13}^T A_{13}\right)^\dagger A_{13}^T(\boldsymbol{u}_{\text{meas}} - \boldsymbol{g}). \quad (5.18)$$

As in (3.22), in (5.18), the matrix $A_{13}^T A_{13} \in \mathbb{R}^{2\mathcal{N}\times 2\mathcal{N}}$ is poorly conditioned if $L \geq \mathcal{N}$ or singular if $L < \mathcal{N}$ and its Moore–Penrose pseudoinverse is calculated with the MATLAB® function `pinv`.

5.1.3. *Step 3.* We solve the BVP in the virtual domain $\Omega_2\backslash\overline{\Omega}_3$ with the known boundary data (5.3) on $\partial\Omega_2$ and the calculated data $\boldsymbol{v}$ on $\partial\Omega_3$ given by (5.18), and evaluate $u_{1_\mathcal{N}}$ and $u_{2_\mathcal{N}}$. We then seek to intersect the level–set iso–curves $u_{1_\mathcal{N}} = u_{\text{int}_1}$ and $u_{2_\mathcal{N}} = u_{\text{int}_2}$ to determine the boundary $\partial\Omega_1$ of the unknown rigid inclusion Ω_1. This task is accomplished via the MATLAB® function `contour`.

We finally demonstrate the capability of the proposed technique to reconstruct rigid inclusions in 3D linear elasticity.

5.1.4. *Example 8.* We consider an example where the curve to be reproduced is a circle of radius 0.5 and all the details of the geometry are the same as in Example 1. The boundary values in (5.2) and (5.3) are taken as $u_{\text{int}_1} = u_{\text{int}_2} = 1$ and $u_{\text{ext}_1} = u_{\text{ext}_2} = 10$. We took $\nu = 0.3$ and $\mu = 1$. The exterior circle $\partial\Omega_2$ has a radius $R = 1$ and the virtual circle $\partial\Omega_3$ has radius 0.3. We took $L = 20$ measurement points on the circle $\partial\Omega_4$ with radius 0.65 for the measurement points. In Step 1, we solved the direct problem $M = N = 20$ and in Steps 2 and 3 we took $\mathcal{N} = 25$ and the solution was evaluated on a 41×41 polar grid in the virtual domain $\Omega_2 \backslash \overline{\Omega}_3$ in order to impose (5.2) and determine the boundary $\partial\Omega_1$ of the rigid inclusion Ω_1. In Figure 10, we present the reconstructed results obtained with no noise and noise $p = 5\%$ and various values of `tol`, which are shown to improve the reconstructed curve. Both iso–curves $u_{1_\mathcal{N}} = u_{\text{int}_1}$ and $u_{2_\mathcal{N}} = u_{\text{int}_2}$ are presented in solid and dashed lines, respectively.

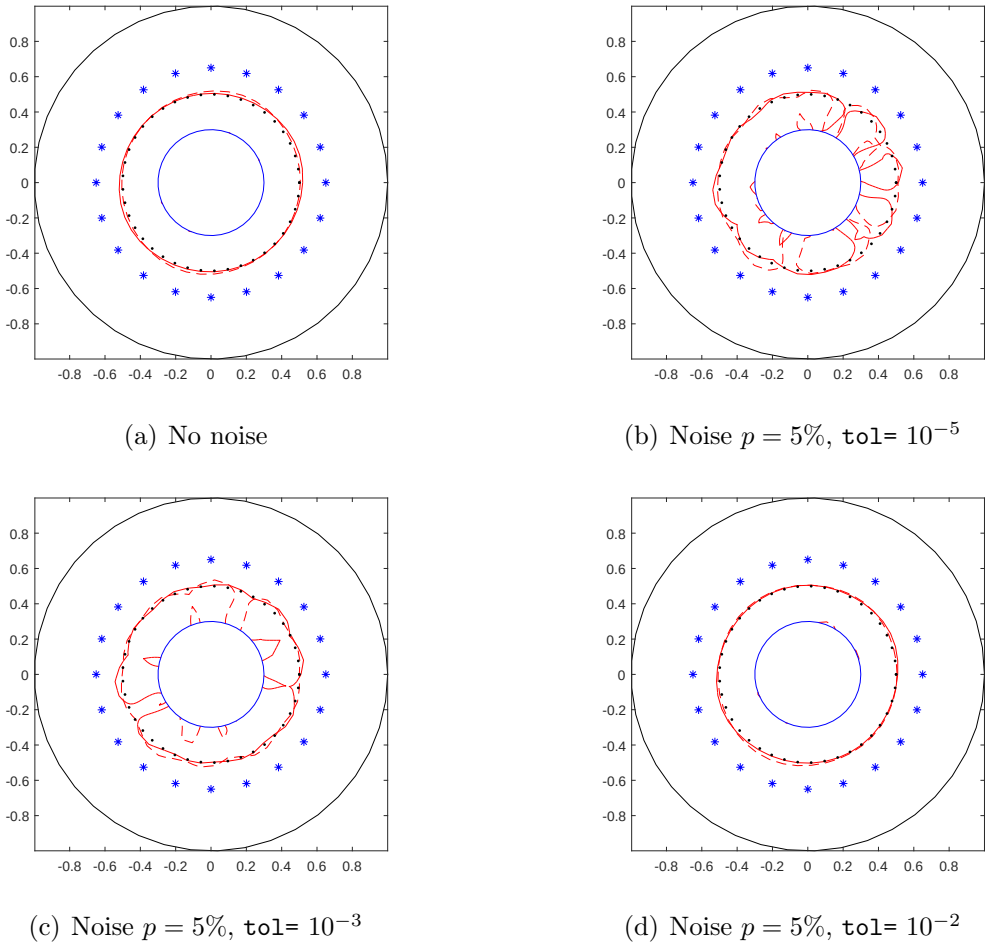

(a) No noise

(b) Noise $p = 5\%$, `tol`$= 10^{-5}$

(c) Noise $p = 5\%$, `tol`$= 10^{-3}$

(d) Noise $p = 5\%$, `tol`$= 10^{-2}$

FIGURE 10. Example 8: Reconstruction of boundary with no noise and noise $p = 5\%$ and various values of `tol`.

5.2. **3D problems.** We now consider the inverse BVP for the Cauchy–Navier equations of linear elasticity in $\mathbb{R}^3$ for the displacement vector $\boldsymbol{u} = (u_1, u_2, u_3)$ given by

$$\left(\frac{2-2\nu}{1-2\nu}\right)\frac{\partial^2 u_1}{\partial x^2} + \frac{\partial^2 u_1}{\partial y^2} + \frac{\partial^2 u_1}{\partial z^2} + \left(\frac{1}{1-2\nu}\right)\frac{\partial^2 u_2}{\partial x \partial y} + \left(\frac{1}{1-2\nu}\right)\frac{\partial^2 u_3}{\partial x \partial z} = 0,$$

$$\frac{\partial^2 u_2}{\partial x^2} + \left(\frac{2-2\nu}{1-2\nu}\right)\frac{\partial^2 u_2}{\partial y^2} + \frac{\partial^2 u_2}{\partial z^2} + \left(\frac{1}{1-2\nu}\right)\frac{\partial^2 u_1}{\partial x \partial y} + \left(\frac{1}{1-2\nu}\right)\frac{\partial^2 u_3}{\partial y \partial z} = 0, \tag{5.19}$$

$$\frac{\partial^2 u_3}{\partial x^2} + \frac{\partial^2 u_3}{\partial y^2} + \left(\frac{2-2\nu}{1-2\nu}\right)\frac{\partial^2 u_3}{\partial z^2} + \left(\frac{1}{1-2\nu}\right)\frac{\partial^2 u_1}{\partial x \partial z} + \left(\frac{1}{1-2\nu}\right)\frac{\partial^2 u_2}{\partial y \partial z} = 0,$$

subject to the Dirichlet BCs

$$u_1 = u_{\text{int}_1} \equiv \text{constant}, \quad u_2 = u_{\text{int}_2} \equiv \text{constant}, \quad u_3 = u_{\text{int}_3} \equiv \text{constant} \quad \text{on} \quad \partial\Omega_1 \tag{5.20}$$

and

$$u_1 = u_{\text{ext}_1}, \quad u_2 = u_{\text{ext}_2}, \quad u_2 = u_{\text{ext}_3} \quad \text{on} \quad \partial\Omega_2, \tag{5.21}$$

where $(u_{\text{ext}_1}, u_{\text{ext}_2}, u_{\text{ext}_3}) \not\equiv (u_{\text{int}_1}, u_{\text{int}_2}, u_{\text{int}_3})$. In the inverse problem, the domain Ω_1 is unknown and to compensate for it we consider the additional measured internal data

$$u_1(\mathbf{x}_\ell) = u_{1_\ell}, \quad u_2(\mathbf{x}_\ell) = u_{2_\ell}, \quad u_3(\mathbf{x}_\ell) = u_{3_\ell} \quad \text{at the points} \quad (\mathbf{x}_\ell)_{\ell=\overline{1,L}} \in \Omega. \tag{5.22}$$

In the MFS, we approximate the solution (u_1, u_2, u_3) of (5.19) by

$$\hat{u}_{1_N}(\boldsymbol{c}, \boldsymbol{d}, \boldsymbol{e}, \boldsymbol{\xi}; \boldsymbol{x}) = \sum_{k=1}^{N} c_k\, G_{11}(\boldsymbol{x}, \boldsymbol{\xi}_k) + \sum_{k=1}^{N} d_k\, G_{12}(\boldsymbol{x}, \boldsymbol{\xi}_k) + \sum_{k=1}^{N} e_k\, G_{13}(\boldsymbol{x}, \boldsymbol{\xi}_k), \tag{5.23a}$$

$$\hat{u}_{2_N}(\boldsymbol{c}, \boldsymbol{d}, \boldsymbol{e}, \boldsymbol{\xi}; \boldsymbol{x}) = \sum_{k=1}^{N} c_k\, G_{21}(\boldsymbol{x}, \boldsymbol{\xi}_k) + \sum_{k=1}^{N} d_k\, G_{22}(\boldsymbol{x}, \boldsymbol{\xi}_k) + \sum_{k=1}^{N} e_k\, G_{23}(\boldsymbol{x}, \boldsymbol{\xi}_k), \tag{5.23b}$$

$$\hat{u}_{3_N}(\boldsymbol{c}, \boldsymbol{d}, \boldsymbol{e}, \boldsymbol{\xi}; \boldsymbol{x}) = \sum_{k=1}^{N} c_k\, G_{31}(\boldsymbol{x}, \boldsymbol{\xi}_k) + \sum_{k=1}^{N} d_k\, G_{32}(\boldsymbol{x}, \boldsymbol{\xi}_k) + \sum_{k=1}^{N} e_k\, G_{33}(\boldsymbol{x}, \boldsymbol{\xi}_k), \tag{5.23c}$$

where the fundamental solution of the Cauchy–Navier system in 3D is

$$G_{11}(\boldsymbol{x},\boldsymbol{\xi}) = \frac{1}{16\pi\mu(1-\nu)}\frac{1}{r}\left[(3-4\nu)+\frac{(x-\xi_x)^2}{r^2}\right], \tag{5.24a}$$

$$G_{12}(\boldsymbol{x},\boldsymbol{\xi}) = \frac{1}{16\pi\mu(1-\nu)}\frac{(x-\xi_x)(y-\xi_y)}{r^3}, \tag{5.24b}$$

$$G_{13}(\boldsymbol{x},\boldsymbol{\xi}) = \frac{1}{16\pi\mu(1-\nu)}\frac{(x-\xi_x)(z-\xi_z)}{r^3}, \tag{5.24c}$$

$$G_{22}(\boldsymbol{x},\boldsymbol{\xi}) = \frac{1}{16\pi\mu(1-\nu)}\frac{1}{r}\left[(3-4\nu)+\frac{(y-\xi_y)^2}{r^2}\right], \tag{5.24d}$$

$$G_{23}(\boldsymbol{x},\boldsymbol{\xi}) = \frac{1}{16\pi\mu(1-\nu)}\frac{(y-\xi_y)(z-\xi_z)}{r^3}, \tag{5.24e}$$

$$G_{33}(\boldsymbol{x},\boldsymbol{\xi}) = \frac{1}{16\pi\mu(1-\nu)}\frac{1}{r}\left[(3-4\nu)+\frac{(z-\xi_z)^2}{r^2}\right], \tag{5.24f}$$

and $G_{21} = G_{12}$, $G_{31} = G_{13}$ and $G_{32} = G_{23}$, $\boldsymbol{x} = (x, y, z)$, $\boldsymbol{\xi} = (\xi_x, \xi_y, \xi_z)$ and $r = |\boldsymbol{x} - \boldsymbol{\xi}|$.

Step 1 is essentially the same as the one described in Section 5.1.1 with the difference that the matrix A in (5.7) is now $6M \times 6N$. Also, in (5.10), we now have $\boldsymbol{u}_{\text{meas}} \in \mathbb{R}^{3L\times 1}$ and $B \in \mathbb{R}^{3L\times 6N}$. Step 2 is mostly the same as in Section 5.1.2, but in (5.11) we have that $A \in \mathbb{R}^{6\mathcal{N}\times 6\mathcal{N}}$ and $\boldsymbol{u} \in \mathbb{R}^{6\mathcal{N}\times 1}$ is defined from

$$u_i = u_{\text{vir}_{1_i}},\ u_{\mathcal{N}+i} = u_{\text{ext}_1}(\boldsymbol{x}_{\mathcal{N}+i}),\ u_{2\mathcal{N}+i} = u_{\text{vir}_{2_i}},\ u_{3\mathcal{N}+i} = u_{\text{ext}_2}(\boldsymbol{x}_{\mathcal{N}+i}),$$

$$u_{4\mathcal{N}+i} = u_{\text{vir}_{3_i}},\ u_{5\mathcal{N}+i} = u_{\text{ext}_3}(\boldsymbol{x}_{\mathcal{N}+i}),\ i = \overline{1,\mathcal{N}},$$

and now the vectors of unknown coefficients are $\boldsymbol{c}, \boldsymbol{d}, \boldsymbol{e} \in \mathbb{R}^{2\mathcal{N}\times 1}$.
Equation (5.13) is replaced by

$$\left(\begin{array}{c}\boldsymbol{c}\\\hline\boldsymbol{d}\\\hline\boldsymbol{e}\end{array}\right) = A^{-1}\boldsymbol{u} = A^{-1}\left[\begin{array}{c}\boldsymbol{u}_\alpha\\\hline\boldsymbol{u}_\beta\\\hline\boldsymbol{u}_\gamma\\\hline\boldsymbol{u}_\delta\\\hline\boldsymbol{u}_\epsilon\\\hline\boldsymbol{u}_\zeta\end{array}\right], \tag{5.25}$$

where the vectors $\boldsymbol{u}_\alpha, \boldsymbol{u}_\gamma$ and $\boldsymbol{u}_\epsilon$ are unknown.
Equation (5.14) is replaced by

$$\tilde{\boldsymbol{u}}_{\text{meas}} = B\,\boldsymbol{c} = BA^{-1}\boldsymbol{u} = [A_1|A_2|A_3|A_4|A_5|A_6]\left[\begin{array}{c}\boldsymbol{u}_\alpha\\\hline\boldsymbol{u}_\beta\\\hline\boldsymbol{u}_\gamma\\\hline\boldsymbol{u}_\delta\\\hline\boldsymbol{u}_\epsilon\\\hline\boldsymbol{u}_\zeta\end{array}\right] = A_{135}\boldsymbol{v} + \boldsymbol{g}, \tag{5.26}$$

where $[A_1|A_2|A_3|A_4|A_5|A_6] = BA^{-1}$ with $A_1, A_2, A_3, A_4, A_5, A_6 \in \mathbb{R}^{3L\times\mathcal{N}}$, $A_{135} = [A_1|A_3|A_5]$, $\boldsymbol{g} = A_2\boldsymbol{u}_\beta + A_4\boldsymbol{u}_\delta + A_6\boldsymbol{u}_\zeta$, and

$$\boldsymbol{v} = \left(\begin{array}{c} \boldsymbol{u}_\alpha \\ \hline \boldsymbol{u}_\gamma \\ \hline \boldsymbol{u}_\epsilon \end{array}\right).$$

Equation (5.18) becomes

$$\boldsymbol{v} = \left(A_{135}^T A_{135}\right)^\dagger A_{135}^T \left(\boldsymbol{u}_{\text{meas}} - \boldsymbol{g}\right), \tag{5.27}$$

and the matrix $A_{135}^T A_{135} \in \mathbb{R}^{3\mathcal{N}\times 3\mathcal{N}}$ is poorly conditioned if $L \geq \mathcal{N}$ or singular if $L < \mathcal{N}$ and its Moore–Penrose pseudoinverse is calculated with the MATLAB® function `pinv`.
In Step 3 we evaluate $u_{1_\mathcal{N}}, u_{2_\mathcal{N}}$ and $u_{3_\mathcal{N}}$ and then seek to intersect the level–set iso–surfaces $u_{1_\mathcal{N}} = u_{\text{int}_1}$, $u_{2_\mathcal{N}} = u_{\text{int}_2}$ and $u_{3_\mathcal{N}} = u_{\text{int}_3}$ to determine the boundary $\partial\Omega_1$to determine the boundary $\partial\Omega_1$ of the unknown rigid inclusion Ω_1. This task is accomplished via the MATLAB® function `isosurface`.

5.2.1. *Example 9.* We study a 3D example where the surface to be reproduced is an ellipsoid with semi–axes lengths of 0.45, 0.45 and 0.6. The exterior sphere Ω_2 has radius $R = 1$ and the virtual sphere Ω_3 has radius 0.35. The boundary values in (5.2) and (5.3) are taken as $u_{\text{int}_1} = u_{\text{int}_2} = u_{\text{int}_3} = 1$ and $u_{\text{ext}_1} = u_{\text{ext}_2} = u_{\text{ext}_3} = 10$. We took $\nu = 0.3$ and $\mu = 1$. We also select $L = 324$ points on the sphere Ω_4 with radius 0.65 for the measurement points in (2.1d). In Step 1 we solved the direct problem with $M = N = 324$ and in Steps 2 and 3 we took $\mathcal{N} = 400$. Finally, the solution was evaluated in the virtual domain $\Omega_2\backslash\overline{\Omega}_3$ on a $21 \times 21 \times 21$ spherical grid in order to impose (5.20) and determine the boundary $\partial\Omega_1$ of the rigid inclusion Ω_1. In Figure 11 we present the reconstructed results obtained with no noise and noise $p = 5\%$ and various values of `tol`, which are shown to improve the reconstructed curve.

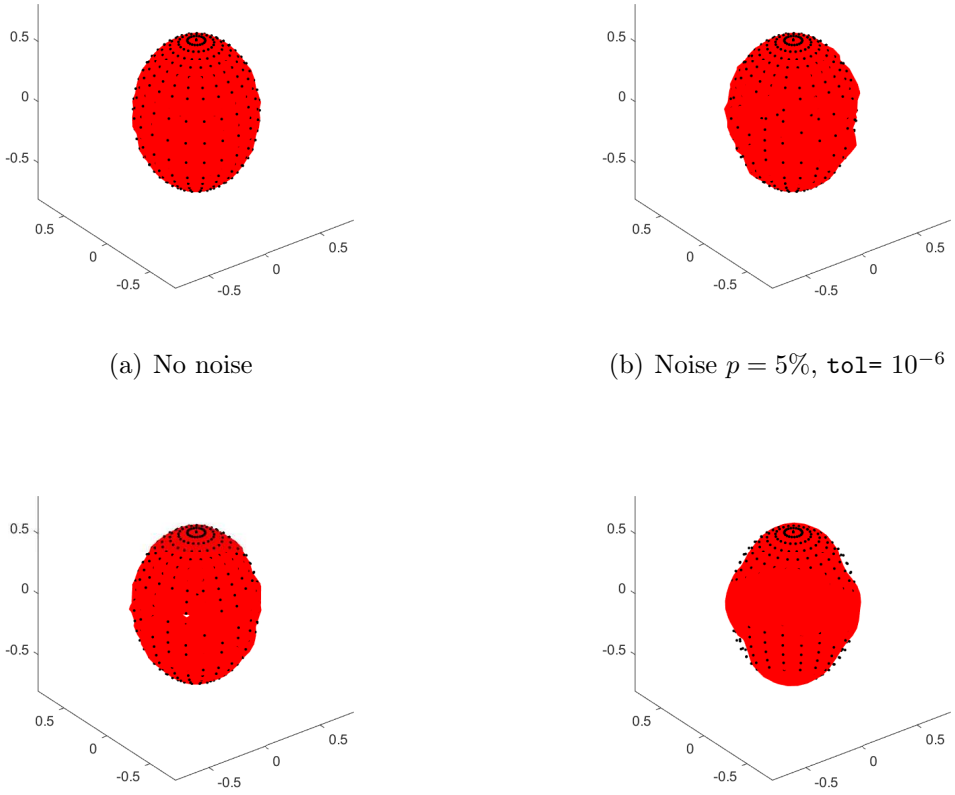

(a) No noise

(b) Noise $p = 5\%$, `tol=` 10^{-6}

(c) Noise $p = 5\%$, `tol=` 10^{-5}

(d) Noise $p = 5\%$, `tol=` 10^{-3}

FIGURE 11. Example 9: Reconstruction of ellipsoidal surface with no noise and noise $p = 5\%$ and various values of `tol`.

6. Conclusions

We have considered the inverse geometric problem (in both 2D and 3D) that requires reconstructing a rigid inclusion Ω_1 concealed in the annular domain in between a known inner curve/surface $\partial\Omega_3$ and an outer curve/surface $\partial\Omega_4$ on which the potential u is measured. Dirichlet data are also supplied through the BC (2.1c). Therefore, in this formulation of the inverse geometric problem we have that $\Omega_3 \subset \Omega_1 \subset \Omega_4 \subset \Omega_2$ and we also assume that the potential u, which is harmonic in $\Omega = \Omega_2 \backslash \overline{\Omega}_1$, can be analytically extended to the domain $\Omega_2 \backslash \Omega_3$. For this particular problem, we have developed a non–iterative MFS. In challenging geometries, the proposed method is not as accurate as the usual nonlinear iterative approach employed by the authors for solving inverse geometric problems [16–19]. The latter approach leads to the solution of systems of nonlinear

equations, see e.g. [19], the solution of which requires the use of sophisticated software. In contrast, the current technique is much easier to implement and less costly and, moreover, lends itself to a simple and effective regularization approach (truncated SVD). The numerical MFS solutions for the Examples 1-3, 6 and 7 possess comparable accuracy with the numerical solutions obtained using the boundary or finite element solutions [27, 28]. Extension to 2D and 3D linear elasticity inverse geometric problems has also been developed. In view of the fact that, for problems in complex geometries, the proposed technique is not as accurate as the nonlinear iterative approach usually employed, in such cases, it could serve as a good initial approximation for other methods such as the ones described in, say, [19]. In the spirit of reproducible research and for the convenience of interested readers, the MATLAB® code of the proposed method for Example 1 is provided at [29]. This also demonstrates the relative ease of implementation of the approach.

The MFS described in this paper can be extended to nonlinear and/or functionally graded materials [23]. Multi–layer composites may also be analysed [3] for identifying anomalies concealed in one of the components of the compound, but the more challenging case of an unknown tumour Ω_1 developing at the interface between two components of the composite is yet to be addressed and will form the objective of a future investigation.

References

[1] C. J. S. Alves and N. F. M. Martins, *Reconstruction of inclusions or cavities in potential problems using the MFS*, in C. S. Chen, A. Karageorghis and Y. S. Smyrlis, Editors, The Method of Fundamental Solutions - a Meshless Method, Dynamic Publishers Inc., Atlanta, 2008, pp 51–73.

[2] C. J. S. Alves and N. F. M. Martins, *The direct method of fundamental solutions and the inverse Kirsch-Kress method for the reconstruction of elastic inclusions or cavities*, J. Integral Equ. Appl., **21** (2009), 153–178.

[3] J. R. Berger and A. Karageorghis, *The method of fundamental solutions for heat conduction in layered materials*, Int. J. Numer. Meth. Eng., **45** (1999), 1681–1694.

[4] F. B. Belgacem, *Why is the Cauchy problem severely ill-posed?*, Inverse Problems, **23** (2007), 823–836.

[5] A. Bogomolmy, *Fundamental solution method for elliptic boundary value problems*, SIAM J. Numer. Anal., **22** (1985), 644-669.

[6] D. Borman, D. B. Ingham, B. T. Johansson and D. Lesnic, *The method of fundamental solutions for detection of cavities in EIT*, J. Integral Equ. Appl., **21** (2009), 381–404.

[7] P. P. Carvalho, A. Doubova, E. Fernandez–Cara and J. Rocha de Faria, *Some new results for geometric inverse problems with the method of fundamental solutions*, Inverse Probl. Sci. Eng., **29** (2021), 131–152.

[8] C. K. Chen and C. R. Su, *Inverse estimation for temperature of outer surface and geometry of inner surface of furnace with two layer walls*, Energ. Conver. Manage., **49** (2008), 301–310.

[9] H. Chen, B. Yu, Z. Liu and H. Zhou, *A non–iterative methodology to reconstruct boundary shapes and conditions in isotropic linear elasticity based on the BEM*, Eng. Anal. Bound. Elem., **153** (2023), 12–24.

[10] S. V. Gavrilov, *Numerical method for solving an inverse problem for Laplace's equation in a domain with an unknown inner boundary*, Comput. Math. Math. Phys., **59** (2019), 59–65.

[11] P. C. Hansen, *The truncated SVD as a method for regularization*, BIT, **27** (1987), 534–553.

[12] P. C. Hansen, *Discrete Inverse Problems: Insight and Algorithms*, SIAM, Philadelphia, 2010.

[13] Y. C. Hon and Z. Wu, *A numerical computation for inverse boundary determination*, Eng. Anal. Boundary Elements, **24** (2000), 599–606.

[14] D. B. Ingham and Y. Yuan *The Boundary Element Method for Solving Improperly Posed Problems*, Computational Mechanics Publications, Southampton, 1994.
[15] A. Karageorghis, D. Lesnic and L. Marin, *The MFS for inverse geometric problems*, in L. Marin, L. Munteanu and V. Chiroiu, Editors, Inverse Problems and Computational Mechanics, Vol. 1, Editura Academiei, Bucharest, Romania, 2011, pp 191–216.
[16] A. Karageorghis, D. Lesnic and L. Marin, *The method of fundamental solutions for the detection of rigid inclusions and cavities in plane linear elastic bodies*, Comput. Struct., **106-107** (2012), 176–188.
[17] A. Karageorghis, D. Lesnic and L. Marin, *A moving pseudo–boundary MFS for three–dimensional void detection*, Adv. Appl. Math. Mech., **5** (2013), 510–527.
[18] A. Karageorghis, D. Lesnic and L. Marin, *The method of fundamental solutions for three–dimensional inverse geometric elasticity problems*, Comput. Struct., **166** (2016), 51–59.
[19] A. Karageorghis, D. Lesnic and L. Marin, *An efficient moving pseudo–boundary MFS for void detection*, Eng. Anal. Bound. Elem., **147** (2023), 90–111.
[20] A. Kirsch and R. Kress, *On an integral equation of the first kind in inverse acoustic scattering*, in J. R. Cannon and U. Hornung, Editors, Inverse Problems, International Series of Numerical Mathematics, vol 77. Birkäuser Basel, 1986, pp 93–102.
[21] A. Kirsch and R. Kress, *An optimization method in inverse acoustic scattering*, in C. A. Brebbia, G. Kuhn and W. L. Wendland, Editors, Boundary Elements IX, Vol. 3: Fluid Flow and Potential Applications, Springer–Verlag, Berlin, 1987, pp. 3–18.
[22] R. Kress, *Inverse Dirichlet problem and conformal mapping*, Math. Comput. Simul., **66** (2004), 255–265.
[23] L. Marin and D. Lesnic, *The method of fundamental solutions for nonlinear functionally graded materials*, Int. J. Solids Struct., **44** (2007), 6878–6890.
[24] R. F. Millar, *The location of singularities of two-dimensional harmonic functions. I: Theory*, SIAM J. Math. Anal., **1** (1970), 333–344.
[25] C. R. Su and C. K. Chen, *Geometry estimation of the furnace inner wall by an inverse approach*, Int. J. Heat Mass Transfer, **50** (2007), 3767–3773.
[26] C. R. Su, C. K. Chen, W. L. Liu and H. Y. Lai, *Estimation of inner surface geometry of furnace wall using inverse process combined with grey prediction model*, Int. J. Heat Mass Transfer, **52** (2009), 3595–3605.
[27] B. Yu, H. L. Zhou, Q. Gao and J. Yan, *Geometry boundary identification of the furnace inner wall by BEM without iteration*, Numerical Heat Transfer, Part A, **69** (2016), 1253–1262.
[28] H. L. Zhou, Y. S. Li, B. Yu and H. L. Chen, *Shape identification for inverse geometry heat conduction problems by FEM without iteration*, Numerical Heat Transfer, Part A, **72** (2017), 628–641.
[29] `https://www.mas.ucy.ac.cy/andreask/Appendix.pdf`

Department of Mathematics and Statistics, University of Cyprus/ Πανεπιστημιο Κυπροϒ,
P.O.Box 20537, 1678 Nicosia/Λευκωσια, Cyprus/Κυπρος
E-mail address: `andreask@ucy.ac.cy`

Department of Applied Mathematics, University of Leeds, Leeds LS2 9JT, UK
E-mail address: `amt5ld@maths.leeds.ac.uk`

Department of Mathematics, Faculty of Mathematics and Computer Science, University of Bucharest, 14 Academiei, 010014 Bucharest, and "Gheorghe Mihoc – Caius Iacob" Institute of Mathematical Statistics and Applied Mathematics of the Romanian Academy, 13 Calea 13 Septembrie, 050711 Bucharest, Romania
E-mail address: `liviu@imsar.bu.edu.ro; marin.liviu@gmail.com`